

**INVESTIGATING RANDOM LASER FROM
ALUMINIUM-DOPED ZINC OXIDE NANORODS**

ABDULLAH TAHA ALI

UNIVERSITI SAINS MALAYSIA

2022

INVESTIGATING RANDOM LASER FROM ALUMINIUM-DOPED ZINC OXIDE NANORODS

by

ABDULLAH TAHA ALI

**Thesis submitted in fulfilment of the requirements
for the degree of
Doctor of Philosophy**

April 2022

ACKNOWLEDGEMENT

Thanks to Allah SWT for giving me the opportunity and help me endlessly in finishing this research. I would like also to express my sincere gratitude to my main supervisor Dr. Wan Maryam Binti Wan Ahmad Kamil for her valuable guidance and support throughout these study years. Without her comments and continuous encouragement, this dissertation would not have been possible. Thank you doctor for having your door open every time I needed help. I would like also to thank my co-supervisors Dr. Naser Mahmoud and Assoc. Prof. Norzaini Zainal for their scholarly guidance and support throughout this study.

My appreciation also goes to the staff of the nano-optoelectronics research laboratory (NOR Lab) and Department of Photonics, National Cheng Kung University, Taiwan for their technical assistance during my laboratory work. My heart gratitude to my family members: my parents, siblings, and my wife for their continuous prayers and endless supported when I needed it. Many thanks to all my friends and colleagues who support and helped me at the school of physics, Universiti Sains Malaysia.

Abdullah Taha Ali

Penang- Malaysia, 2022

TABLE OF CONTENTS

ACKNOWLEDGEMENT	ii
TABLE OF CONTENTS	iii
LIST OF TABLES	viii
LIST OF FIGURES	ix
LIST OF SYMBOLS	xiv
LIST OF ABBREVIATIONS	xvi
LIST OF APPENDICES	xviii
ABSTRAK	xix
ABSTRACT	xxi
CHAPTER 1 INTRODUCTION	1
1.1 Introduction	1
1.2 Problem Statement	3
1.3 Objectives of This Study	6
1.4 Originality of This Research	6
1.5 Thesis Outline	7
CHAPTER 2 LITERATURE REVIEW AND THEORETICAL BACKGROUND	8
2.1 Introduction	8
2.2 Fundamental Properties of ZnO	8
2.2.1 The Crystalline Structure and Lattice Parameters.....	9
2.2.2 Optical Properties.....	11
2.3 Methods to Synthesize ZnO Nanostructures.....	13
2.3.1 Chemical Bath Deposition	14
2.4 Metal-doped ZnO Properties.....	17
2.4.1 Al-doped ZnO Nanostructures	18

2.4.1(a)	Effects of Al-Doping on The Morphological Properties.....	18
2.4.1(b)	Effects of Al-Doping on The Optical Properties.....	20
2.5	Random Lasers.....	21
2.6	Key Principles of Random Laser	23
2.6.1	Gain Medium	23
2.6.2	Coherent and Incoherent of Optical Feedback.....	24
2.6.3	Threshold Condition	26
2.7	Controlling Random Laser Properties.....	28
2.7.1	Laser Tunability	28
2.7.2	Laser Directionality.....	29
2.8	Review of Random Laser in ZnO Nanostructures	30
2.9	Tunability of Random Laser in ZnO Nanostructures.....	34
2.10	Random Laser in Al-doped ZnO Nanostructures.....	38
2.11	SiO ₂ -Capped ZnO Properties and Their effects on Optical Confinement.....	39
2.12	Random Laser Applications.....	42
2.13	Summary	45
CHAPTER 3 METHODOLOGY AND INSTRUMENTATION.....		46
3.1	Introduction	46
3.2	Preparation of ZnO Seed Layer.....	48
3.2.1	Substrate Cleaning	49
3.2.2	Radio Frequency Sputtering.....	50
3.2.3	Annealing Treatment.....	52
3.3	Synthesis of Al-doped ZnO Nanorods via Chemical Bath Deposition.....	53
3.3.1	Growth of Al-doped ZnO Nanorods at Different Al Concentrations.....	54
3.3.2	Growth of Al-doped ZnO Nanorods at Different Temperatures.....	56

3.4	Capping Method.....	57
3.4.1	SiO ₂ -capped ZnO Nanorods.....	57
3.4.2	SiO ₂ -capped Al-doped ZnO Nanorods.....	57
3.5	Characterization Techniques	58
3.5.1	Morphological properties	58
3.5.1(a)	Field Emission Scanning Electron Microscopy and Energy-Dispersive X-ray Spectroscopy Measurements.....	58
3.5.1(b)	Atomic Force Microscopy.....	62
3.5.2	Structural properties	63
3.5.2(a)	X-ray Diffraction Measurement	63
3.5.2(b)	Transmission Electron Microscopy Measurement.....	64
3.5.3	Electrical properties	66
3.5.3(a)	Hall Effect Measurement	66
3.5.4	Optical properties	67
3.5.4(a)	Ultraviolet Visible Spectroscopy Measurement.....	67
3.5.4(b)	Photoluminescence Spectroscopy Measurements.....	69
3.5.5	Random Laser Measurement.....	70
3.6	Simulation and Image Processing Software.....	71
3.6.1	Simulation Software.....	71
3.6.2	Image Processing (ImageJ software)	73
3.7	Summary	74
CHAPTER 4 RESULTS AND DISCUSSION.....		75
4.1	Introduction	75
4.2	Characterization of ZnO seed layer.....	75
4.2.1	Morphological Properties.....	76
4.2.2	Structural Properties.....	79
4.3	Al-doped ZnO Nanorods at Different Al Concentrations	82

4.3.1	Morphological Properties.....	82
4.3.2	Structural Properties.....	85
4.4	Al-doped ZnO Nanorods Prepared at Different Growth Temperatures.....	87
4.4.1	Morphological Properties.....	87
4.4.2	Structural Properties.....	90
4.4.3	Optical properties	91
4.4.3(a)	PL Spectroscopy.....	91
4.4.3(b)	Optical Absorption Spectra	95
4.4.4	Random Laser Properties	96
4.5	SiO ₂ capped-ZnO Nanorods.....	102
4.5.1	Morphological Properties.....	103
4.5.2	Structural Properties.....	105
4.5.3	Optical Properties.....	107
4.5.3(a)	PL Spectroscopy.....	107
4.5.3(b)	Optical Absorption Spectra	108
4.5.4	Random Laser Properties	109
4.5.5	Optical Simulation Results.....	112
4.6	SiO ₂ capped Al-doped ZnO Nanorods.....	113
4.6.1	Morphological Properties.....	114
4.6.2	Structural Properties.....	114
4.6.3	Optical Properties.....	116
4.6.4	Random Laser Properties	117
CHAPTER 5 CONCLUSIONS AND FUTURE WORKS		123
5.1	Conclusions	123
5.2	Recommendations for Future Researches.....	126

REFERENCES..... 127

APPENDICES

LIST OF PUBLICATIONS

LIST OF TABLES

	Page
Table 2.1	Summary of the basic physical parameter of ZnO [60]. 11
Table 3.1	RF sputtering conditions for ZnO seed layer on glass substrate..... 52
Table 4.1	EDX results of the atomic percentage of elements in each sample. 90
Table 4.2	Comparison of Al atomic percentage with the extrapolated optical band gap and carrier concentration of AZO NRs..... 94
Table 4.3	Summarized values of random laser in ZnO NRs, AZO NRs, SiO ₂ capped-ZnO NRs, and SiO ₂ capped-AZO NRs 121
Table 4.4	Comparing the performance of random laser results of ZnO NRs with other researchers 122

LIST OF FIGURES

		Page
Figure 2.1	Stick-and-ball representation of ZnO crystal structures. (a) cubic rocksalt (B1), (b) zinc blende (B3), and (c) wurtzite (B4). Shaded gray and black spheres denote Zn and O atoms, respectively[57].	10
Figure 2.2	FESEM cross-sectional and top-view images of ZnO nanostructures doped with (a, d) 1% Al; (b, e) 3% Al. (b) [33].	20
Figure 2.3	FESEM images of the surface morphology of ZnO nanostructures doped with (a) 5% and (b) 7% Al [33].	20
Figure 2.4	(a) Schematic diagram of Fabry-Perot laser consists of two mirrors and gain medium (b) laser output for conventional laser [112].	22
Figure 2.5	Spectra of emission from ZnO powder when the excitation intensity is (from bottom to top) 400, 562, 763, 875, and 1387 kW/cm ² [113].	31
Figure 2.6	Scanning electron micrograph of sub micrometre-sized ZnO particles (a) before and (b) after laser-induced melting. (c) Fluorescence image of a polymer particle (arrow) and (d) emission intensity distribution of a ZnO particle film including a point defect [168].	32
Figure 2.7	Emission spectra measured at (a) defect-free and (b) defect sites (arrows 2 and 1 in figure 2.4(d)). The excitation intensities were 0.5, 1.0, and 2.0 times of each threshold from bottom to top. The insets in each figure show the excitation intensity dependences of peak intensities. Arrows indicate the threshold intensity [168].	33
Figure 2.8	(a) Lasing action before stretching. Lasing action of stretching length (b) 10%, (c) 20%, and (d) 30%. (e) Detected times versus lasing mode number before stretching. Detected times versus lasing mode number of stretching length (f) 10%, (g) 20%, and (h) 30% [37].	35
Figure 2.9	(a) Evolution of emission spectra obtained for the N-doped sample under different pump intensities. (b) Light–light curves of the samples. (c) Evolution of emission spectra obtained for the Fe-doped sample at under different pump intensities. (d) Light–light curves of the samples [177].	37

Figure 2.10	Schematic representation for the excitation and emission processes responsible for the enhancement of the UV emission intensity[194].	41
Figure 2.11	RL emission spectra of human colon tissues infiltrated with a concentrated laser dye, namely R6G. (a) Two typical RL emission spectra from a healthy, grossly uninvolved tissue (blue), of which microscopic image is shown in (b). (c) and (d), a malignant colon tissue. There are more lines in the laser emission spectra in (c) (red) that are due to more resonators in the tumor; these are caused by the excess disorder that is apparent in (d) [129].....	44
Figure 2.12	LSP optical set-up. The intensity of the laser beam is controlled by means of a half-wave plate and a polarizing beam splitter. Two mirrors are used to orientate the beam towards the object. Lens L1 is used to control the beam width at the diffractive [199].....	44
Figure 3.1	Flow chart summarising the experimental flow.....	47
Figure 3.2	ZnO Seed layer preparation steps.	48
Figure 3.3	Microscope glass slides used as substrate.....	49
Figure 3.4	(a) a photograph of Edward A500 UK sputtering system, and (b) schematic diagram of RF-sputtering.	51
Figure 3.5	(a) Tube furnace used and (b) schematic diagram of the tube furnace for annealing treatment.	53
Figure 3.6	The three steps of the mixing the three of chemical solutions.....	55
Figure 3.7	general steps of the chemical bath deposition (CBD).....	56
Figure 3.8	(a) Schematic diagram of the main components of a FESEM, (b) Photograph of model FEI Nova NanoSEM 450 and Zeiss Supra 35VP, and (c) Signals generated when the electron beam strikes the specimen.....	61
Figure 3.9	Schematic diagram of EDX- analyzer.....	61
Figure 3.10	Schematic diagram of atomic force microscopy (AFM), and (b) photograph of AFM.....	62
Figure 3.11	(a) Schematic diagram of the X-ray diffraction process, (b) Photograph of PANalytical X Pert PRO XRD diffractometer and (c) Schematic diagram of Bragg's law.	64
Figure 3.12	The photograph and schematic diagram of transmission electron microscopy (TEM) system.....	66

Figure 3.13	Schematic illustration of Hall Effect measurement.	67
Figure 3.14	Illustration of the inner components of the Cary Series 5000 UV vis–NIR spectrophotometer.....	68
Figure 3.15	3D schematic diagram of μ -PL spectroscopy system	70
Figure 3.16	Data analysis using ImageJ.	74
Figure 4.1	(a-d) 2D AFM images and (e-h) FESEM with inset cross sections images of the ZnO seed layers with seed annealing temperatures from 150 °C to 450 °C.....	78
Figure 4.2	EDX results of the ZnO seed layer at different annealing temperatures of (a)150 °C, (b) 250 °C, (c) 350 °C and (d) 450 °C.	79
Figure 4.3	The XRD pattern for the ZnO Seed layer annealed at different temperatures.	81
Figure 4.4	The FESEM images (top view and cross-section), and EDX analysis of the AZO NRs at different Al concentrations.	84
Figure 4.5	Graph of the average nanorod height, diameter, and density with an increasing of Al concentration.	85
Figure 4.6	XRD spectra of AZO-NRs at different Al concentrations.....	86
Figure 4.7	Top view (a-f) and Cross-sectional view (Inset) FESEM images of the AZO NRs fabricated with bath temperatures of 80°C, 90°C, 100°C, 110°C, 120°C and 130°C, respectively. Images are then analyzed by ImageJ to determine the average diameter.....	88
Figure 4.8	Graph of the average nanorod height, diameter, and density with increasing growth temperature.....	88
Figure 4.9	Top view FESEM images of AZO NRs fabricated with temperatures (a)140°C and (b)150°C.....	89
Figure 4.10	XRD spectra of AZO NRs at different growth temperatures.....	91
Figure 4.11	Photoluminescence spectra of AZO NRs at different growth temperatures.	94
Figure 4.12	(a) Changes in bandgap energy at various growth temperatures, and (b) optical band gap linear shift against carrier concentration ($ne^{2/3}$).....	95
Figure 4.13	(a) Absorption spectra of AZO NRs at different growth temperatures, (b) Plot of $(\alpha hv)^2$ versus hv	96

Figure 4.14	Optical pumping power dependence lasing measurement from AZO-NRs with different growth temperatures of (a) 80°C, (b),90°C, (c)100°C, (d)110°C, (e)120°C and, (f)130°C, respectively. Inset: FWHM of the highest intensity lasing mode that appeared at threshold at different pump powers.	99
Figure 4.15	Integrated lasing intensity of AZO-NRs as a function of excitation power for each doped sample at different growth temperature.....	100
Figure 4.16	(a) RL emission spectra of AZO-NRs at different doping percentage (at. %), under fixed excitation power of 1mW, and (b) the mean lasing peaks as a function of the doping percentage (at. %).....	101
Figure 4.17	FESEM, top view, and cross-section of (a, e) bare ZnO NRs and SiO ₂ capped ZnO NRs at different thicknesses: (b, f) 25 nm, (c, g) 75 nm, and (d, h) 100 nm, respectively.	104
Figure 4.18	TEM images of the (a) bare ZnO NRs and SiO ₂ capped ZnO NRs with (b) 25 nm, (c) 75 nm, and (d) 100 nm of SiO ₂	105
Figure 4.19	XRD data of (a) bare ZnO NRs and SiO ₂ capped ZnO NRs at different thickness of: (b) 25 nm, (c) 75 nm, and (d) 100 nm.....	106
Figure 4.20	Photoluminescence spectra of (a) bare ZnO NRs, and SiO ₂ capped ZnO NRs at different thickness of: (b) 25nm, (c) 75nm, and (d) 100nm.	108
Figure 4.21	Absorption spectra of the glass substrates with ZnO-seed layer, ZnO NRs, and SiO ₂ -coated ZnO NRs at different thicknesses: 25 nm, 75 nm, and 100 nm.	109
Figure 4.22	RL measurements for ZnO NRs and SiO ₂ -coated ZnO NRs at different thicknesses: (a) bare ZnO NRs, (b)25 nm, (c)75 nm, and (d)100 nm. (e) Peak emission intensities, and (f) FWHM of emission spectra of all samples as a function of the excitation power.	111
Figure 4.23	(Color online) Nanorod waveguide intensity distribution of the cross-section NRs structure (300 nm diameter and 2600nm height) at the wavelength of 355 nm. Two modes are shown in (a) uncoated ZnO and (b) SiO ₂ coated ZnO.....	113
Figure 4.24	FESEM, top view, and cross-section of (a) S-AZO1, (b) S-AZO2, (c) S-AZO3, (d) S-AZO4.....	114
Figure 4.25	XRD spectra of SiO ₂ capped AZO NRs samples.....	115
Figure 4.26	Photoluminescence spectra of SiO ₂ capped AZO NRs at different growth temperatures.	117

Figure 4.27	RL measurements for the 100nm SiO ₂ -capped AZO NRs at different growth temperatures: (a) S-AZO1, (b) S-AZO2, (c) S-AZO3, and (d) S-AZO4. (e) FWHM of emission spectra, and (f) Peak emission intensities of all samples as a function of the excitation power.....	119
Figure 4.28	RL emission spectra of SiO ₂ -capped AZO-NRs pumped at a fixed excitation power of 0.8mW.....	120

LIST OF SYMBOLS

Å	Angstrom, 10^{-10} m
a.u.	Arbitrary unit
C	Lattice parameter of Miller indices
°C	Celsius
d	Interplanar spacing in the crystalline material
eV	Electron volt
H	Hour
Hz	Hertz
K	Kelvin
kHz	Kilo hertz
L	Laser cavity length
n	Integer
nm	Nanometer, 10^{-9} m
meV	Milli-electron volt, 10^{-3} eV
ml	Milliliter
Min	Minutes
mW	Milliwatts
mA	Milli ampere
Mbar	Millibar
μm^2	Micrometer square
mJ/cm^2	Milli joule per square centimeter
θ	Diffraction angle
μ	Micro, 10^{-6} m
λ	Wavelength
W	Watt

sccm	Standard cubic centimeters per minute
F	Lorentz force
q	Charge
V	Volt
B	Magnetic Field
E _g	Energy bandgap
T	Temperature
m* _e	Effective electron mass
n _e	Carrier density

LIST OF ABBREVIATIONS

Al	Aluminum
ASE	Amplified spontaneous emission
Avg.	Average
at. %	Atomic ratio
AFM	Atomic force microscope
AZO	Aluminum doped-zinc oxide
CBD	Chemical bath deposition
CVD	Chemical vapor deposition
CO ₂	Carbon dioxide
Cu	Copper
Cu-K α	Copper K (alpha)
DLE	Deep level emission
DI-Water	De-ionized water
EDX	Energy Dispersive X-Ray
FESEM	Field emission scanning electron microscopy
FWHM	Full width of half maxima
GaN	Gallium nitrate
H ₂	Hydrogen gas
HMT	Hexamethylenetetramine
ITO	Indium tin oxide
LASER	Light amplification by stimulated emission of radiation
MBE	Molecular beam epitaxy
mbar	millibar
MOCVD	Metal-organic chemical vapour deposition
MOVPE	Metal-organic vapour-phase epitaxy

NBE	Near band edge
NRs	Nanorods
NIR	Near infrared
N ₂	Nitrogen gas
Nd:YAG	Neodymium-doped yttrium aluminum garnet
O ₂	Oxygen
PLD	Pulse laser deposition
PL	Photoluminescence
PVD	Physical vapour deposition
RF	Radio frequency
RT	Room temperature
RL	Random laser
SEM	Scanning electron microscopy
SiO ₂	Silicon dioxide
SPR	Surface plasmon resonance
TEM	Transmission electron microscopy
VLS	Vapour liquid solid
XRD	X-ray diffraction
ZnO	Zinc oxide
1D	One dimensional
2D	Two dimensions
3D	Three dimensions
μ-PL	Micro-photoluminescence

LIST OF APPENDICES

Appendix Waveguides; Model and simulations by COMSOL multi-physics

KAJIAN LASER RAWAK DARIPADA NANOROD ZINK OKSIDA TERDOP ALUMINIUM

ABSTRAK

Dalam penyelidikan ini, sifat laser rawak (RL) dikaji daripada nanorod Zink oksida terdop Aluminium (AZO-NRs) yang disediakan menggunakan kaedah pemendapan rendaman kimia (CBD), kemudian dilitupi dengan lapisan silikon dioksida (SiO_2) yang dihasilkan menggunakan kaedah percikan frekuensi radio. Penyepaduan kedua-dua pendekatan ini bertujuan untuk menambahbaik pancaran RL ultraungu daripada AZO NRs disamping membolehkan keadaan laser boleh tala dengan melaraskan parameter pendopan. Oleh itu, penyelidikan ini dibahagikan kepada tiga bahagian. Bahagian pertama adalah untuk menentukan keadaan pertumbuhan optimum untuk AZO NRs. Bahagian kedua adalah untuk mengenal pasti sifat pancaran RL daripada AZO NRs. Bahagian ketiga memfokuskan kajian berkenaan kesan lapisan penutup SiO_2 pada zink oksida (ZnO) NRs dan AZO NRs dengan mempelbagaikan ketebalan SiO_2 . Sifat struktur, morfologi, optic dan elektrik sampel-sampel turut dikaji untuk kejelasan hasil kajian. Penigkatan kepekatan Al ketika proses CBD membawa kepada perubahan kadar pertumbuhan dan menunjukkan perubahan kepada saiz NRs. Ini merupakan satu masalah dalam mengenal pasti sifat RL yang dihasilkan melalui kaedah pendopan kerana terdapat perubahan pada morfologi atau struktur yang ketara. Percubaan berbeza dalam meningkatkan peratusan dopan Al dilakukan dengan mengubah suhu CBD pada kepekatan 5mM, yang telah dikenal pasti sebagai kepekatan larutan tertinggi yang tidak mengubah morfologi AZO NRs, telah menyelesaikan masalah ini. Sampel dengan nisbah dopan yang tertinggi (1.72 at.%) menunjukkan nilai ambang laser terendah iaitu 0.192 mW

beserta lebar spektrum yang kurang daripada 0.08 nm. Tambahan pula, AZO NRs menunjukkan potensi menggunakan dopan sebagai parameter penalaan untuk RL, di mana ~ 7.3 nm anjakan merah puncak laser dilihat dengan peningkatan dopan (0.9 - 1.72 at.%). Pancaran RL bagi ZnO NRs yang ditutup dengan 100 nm SiO₂ menunjukkan kekuatan pancaran 30 kali ganda lebih baik berbanding dengan ZnO NRs yang terdedah dan puncak RL hampir menindas puncak pancaran spontan sepenuhnya pada nilai ambang (~1.2 mW). Sampel dengan peratusan dopan Al tertinggi yang ditutup dengan 100 nm SiO₂ menunjukkan pancaran RL pada pam ambang rendah sebanyak 0.21 mW dengan lebar spektrum kurang daripada 0.2 nm, dan puncak sinaran adalah 60 kali ganda lebih kuat berbanding dengan ZnO NR yang terdedah. Akhir sekali, AZO NRs yang ditutup SiO₂ menunjukkan keupayaan untuk menala puncak sinaran laser sehingga 5.15 nm. Secara keseluruhannya, kajian ini memberikan penekanan pada AZO NRs, ZnO NRs yang ditutup SiO₂ dan AZO NRs yang ditutup SiO₂ sebagai calon yang berpotensi sebagai peranti RL dan aplikasinya.

INVESTIGATING RANDOM LASER FROM ALUMINIUM-DOPED ZINC OXIDE NANORODS

ABSTRACT

In this research, random lasing (RL) properties are investigated from Aluminium-doped Zinc oxide (AZO) nanorods (NRs) prepared by chemical bath deposition (CBD) method, then capped with silicon dioxide (SiO_2) layer by radio frequency sputtering technique. The integration of the two approaches aims to improve ultraviolet RL emission from AZO NRs whilst enabling lasing tunability by adjusting doping parameters. Therefore, this work is divided into three parts. The first part is to determine the optimal growth conditions for AZO NRs. The second part is to identify RL emission properties from AZO NRs. The third part focuses on investigating the effect of having SiO_2 capping layer on ZnO NRs and AZO NRs by varying SiO_2 thicknesses. The structural, morphological, optical and electrical properties of the samples were also investigated for clarity. Increasing Al concentration during the CBD process led to a decrease in the growth rate and showed an increase in the size of NRs. This becomes a problem in identifying the RL properties that is due to doping since there is significant changes in morphology or structure. A different attempt in increasing the Al doping percentage was done by varying the CBD temperature at a fixed concentration of 5mM, this concentration, which was determined to be the maximum concentration that preserves the morphology of AZO NRs, demonstrated to solve this problem. The sample with the highest doping (1.72 at.%) exhibited the lowest lasing threshold of 0.192 mW with spectral width less than 0.08 nm. Furthermore, the AZO NRs showed the potential of utilizing dopants as a tuning parameter for RL, whereby ~ 7.3 nm redshift of the lasing peak was observed with

increasing doping (0.9 – 1.72 at.%). The RL emission from ZnO NRs capped with 100 nm of SiO₂ showed 30 times stronger emission compared to bare ZnO NRs and the RL peaks almost suppressed the spontaneous emission peak completely upon reaching threshold (~1.2 mW). The sample with highest Al doping that was capped with 100 nm of SiO₂ exhibits RL emission at a low pumping threshold of 0.21 mW with a spectral width of less than 0.2 nm, and lasing peaks are 60 times stronger compared to the bare ZnO NRs. Finally, the SiO₂ capped AZO NRs demonstrated the ability to tune the lasing peaks to about 5.15 nm. Overall, this study provided an emphasis on AZO NRs, SiO₂ capped-ZnO NRs, and SiO₂ capped-AZO NRs as potential candidates for RL devices and their applications.

CHAPTER 1

INTRODUCTION

1.1 Introduction

By virtue of light scattering from the surface of objects, we can see the world. Although light scattering is very useful in our daily life, it is considered to be detrimental in some scientific applications. For example, for a conventional laser system with a gain medium that amplifies light by stimulated emission and a cavity that provides resonant feedback, scattering would remove photons from the laser cavity thus reducing the laser performance.

In a nanostructure scattering environment, however, the light generated in a gain medium can be scattered and amplified multiple times before exiting the gain media, producing stimulated emission. Ambartsumyan and co-workers suggested this type of lasing in 1966, in which one of the Fabry—Perot cavity's mirrors was replaced with a scattering surface [1]. This is where non-resonant feedback lasers are originated. Letokhov proposed in 1968 that scatters can provide feedback for stimulated emission, obviating the necessity for reflective components in a lasing system completely [2]. In 1995, stimulated emission that is based on light scattering was named as a random laser (RL). Scattering can provide intensity feedback depending on whether the scattered light can return to its original position; consequently, RLs are classed as coherent RLs or incoherent RLs [3].

Among the materials employed as a gain medium for RL, ZnO nanostructures stand out as a versatile option that can be optically or electrically pumped and has been included in a wide range of hosts. In addition to acting as the scattering medium, ZnO

RL have demonstrated great efficiency under single and multiple photon stimulation, allowing for a wide variety of excitation wavelengths. Moreover, ZnO RL has been shown to hold important applications from bio-imaging, multiphoton microscopy, laser therapy and optical storage at high-resolution levels. Nowadays, remarkable progress in developing short-wavelength emitters based on wide band-gap semiconductors has led to the choice of using ZnO in the field of photonics and optoelectronics [4]. Many physical and chemical fabrication techniques have been utilized to achieve ZnO nanostructures including molecular beam epitaxy, metal organic chemical vapour deposition, vapour liquid solid mechanism, and pulsed laser deposition [5–8]. Complex processes, sophisticated equipment, high operating temperatures, and toxic chemicals used in these processes make large-scale commercialization challenging and expensive. On the other hand, hydrothermal technique known as chemical bath deposition (CBD) is known for its simplicity as it is possible to operate at low temperature using basic equipment that is available in any standard research facility [9–11].

The lasing characteristic of ZnO micro/nanostructures is generally classified by two feedback mechanisms namely microcavity laser and lasing [12]. In microcavity lasing, light confinement is attributed to the high refractive index of ZnO and the light can be amplified within a single ZnO micro/nanocrystal [13]. On the other hand, lasing is a mechanism closely related to scattering and localization of light in disordered media [14]. Thus, one can expect the lasing properties varies with morphological properties. In this study, we are presenting two types of ZnO based RLs. One is using aluminum doping and the other with SiO₂ capping to optimize the RL in terms of lowering the threshold power, increasing the emission intensity, and providing wavelength tunability.

1.2 Problem Statement

Today, semiconductor products have disseminated throughout the world and permeate our daily lives profoundly. Previous studies of RL have successfully demonstrated room-temperature UV lasing emission utilizing a popular low-cost method for producing ZnO NRs [15–18]. Furthermore, developing such low-cost synthesizing approach is a potential solution for industrial RL devices. However, due to the randomness of the scattering events as RL is an open cavity-based laser, achieving a low threshold has been an ongoing problem. More specifically the problem is that the RLs usually have relatively high lasing thresholds due to scattering losses (due to relying on scattering to confine the light). Another issue is spontaneous emission background, which is frequently accompanied by an increase in pumping power regardless of the material used. Therefore, to develop a narrow linewidth and high intensity RL with relatively low threshold, various methods have been proposed such as by optimizing surface morphology of ZnO NRs [19], optimizing annealing conditions in ZnO NRs [17,18], using a high concentration of ZnCdSeS/ZnS alloyed quantum dot-doped polymer-dispersed liquid crystals [20], forming defect pits in thin films [21], coupling with Fabry-Perot resonance modes induced in nanocolumns [22], utilizing excitons [23], enhancing optical confinement formed by tapered nanowires [13], and fluorescence resonance energy transfer coupled with light scattering [24]. The techniques used in prior works to reduce the lasing threshold may add complexities to the high-cost fabrication methods.

In this work, we attempt a new approach to overcome this problem through doping ZnO with aluminium (Al) atoms which is a common material to doped with ZnO in CBD process because the ionic radius of Al^{3+} (0.53 Å) is smaller than that of Zn^{2+} (0.74 Å). In terms of structural and optical properties, Al doped in ZnO plays a

critical role in changing the properties of ZnO (the gain media of our RL). It is also possible that higher doping concentration leads to a band of energies from impurity states and hence exciting more photons with lower pumping power [25,26].

Several issues regarding *in-situ* doping with CBD must be addressed. The most dominant issue is that doping may change the growth mechanism. Transformation from vertical ZnO NRs to ZnO nanoplate structures was observed in CBD methods when the Al content was above 5 wt.% [33]. A decrease in growth rate was also observed with increasing Al dopants due to the presence of Al(OH)_4^- , which is impeding the growth along the c-axis, as well as decelerating the growth by the pronounced precipitation of the solution [34]. Doping that changes morphology hinders the possibility of utilizing doped nanostructures for optoelectronic devices. In this work, we will attempt to fabricate well-aligned AZO-NRs using CBD formed at different growth temperatures instead of changing Al concentration inside of the growth solution since the Al concentration in the AZO NRs will increase with increasing growth temperature, due to the increased growth rate of the inserted Al–O monocycle [35].

A considerable amount of research on tunable RLs has been conducted to move RLs from theory to practical application [36–41]. Most tuning parameters are external controls, like using temperature, voltage, or electromagnetic wave, etc., to tune the emission wavelength of RLs. However, this is not considered as suitable controls in terms of embedded optoelectronic devices (like photodetectors for example). Moreover, reported work showed that the intensity of the RL decreases as the temperature or applied voltage increases, which limits the RL for practical use. Therefore, tuning RL emission using doping technique is more reliable in terms of

low-cost, applicability and adaptability to existing optoelectronic devices. Hence, other than the attempt to decrease the lasing threshold, the works proposed in this thesis also aims to utilise the AZO NRs RLs as a tuneable UV RL.

Laser characterizations are generally determined by the optical properties of the resonator. In the case of NRs, the feedback mechanism is related to the model of Fabry–Perot cavities for longitudinal modes [42,43], and guided modes [43,44]. However, distinguishing between feedback mechanisms in ZnO nanostructures is a challenging task, especially in nanorod structures grown with various orientations [45]. Another problem relates to limitations of lasing efficiency in the nanostructure medium and this is resonator losses, which are influenced by the size of the NRs as well as the reflectivity of the end faces (like the reflectivity of mirrors at each ends of the resonator in traditional resonators) [44]. Hence, according to the Fabry–Perot model, the bare ZnO rods alone could be bad resonators. It is possible that silicon dioxide (SiO₂)-capped ZnO reduces the Fresnel reflection effect on the NRs surfaces, thus expanding the resonator properties offered by ZnO NRs [46]. Thus, we ventured into SiO₂-capped technique on ZnO NRs and AZO-NRs to improve the guided modes during the stimulated emission inside the nanorod as a method for optimizing RL intensity. As a result, the performance of RL will have better efficiency at a lower threshold. This is especially beneficial as we move towards electrically pumped RLs.

1.3 Objectives of This Study

The main objectives are outlined below:

- 1- To characterize the effect of the Al concentration and growth temperature on the structural and optical properties of the aligned ZnO NRs synthesized via CBD technique.
- 2- To demonstrate a tuneable random lasing spectrum with narrow linewidth under low threshold using AZO NRs.
- 3- To investigate the improvement in lasing emission by increasing light confinement in AZO NRs through capping with SiO₂.

1.4 Originality of This Research

The originality of this study is based on the following points:

1. No previous report on the doping ZnO NRs by increasing the chemical bath temperature have been reported. Hence, the method of maintaining the molarity but increasing the temperature to increase the amount of Al doping in ZnO is a new method proposed through this project.
2. Narrow bandwidth and low emission background under low lasing threshold introduced by AZO NRs by utilising doping was developed.
3. A new approach to tuning RL wavelength by adjusting the Al doping ratio in ZnO NRs.
4. No previous reports can be found about SiO₂ quasi-layer capped on ZnO rods to optimise RL emission. The novelty in confining the light by capping just a portion of the NRs improved the lasing emission.

1.5 Thesis Outline

This work consists of five chapters. Chapter one discusses general overview of the subject, problem statement, objectives, and originality of the thesis. Chapter two provides the literature review and theoretical background ZnO material, metal-doped ZnO, different techniques of fabrication Al-doped ZnO and current unsolved problems related to random lasing, the concept of random lasing, different techniques for controlling RL, and overview of SiO₂-capped ZnO properties and their effects on RL gain media. Chapter three describes the methodology and the instrumentation used for material characterization and RL measurement and analysis. Chapter four presents the results of the work starting with discussion and analysis of the structural, optical, and electrical properties of all samples. This is followed with results related to RL emission and discussion of the results obtained. Chapter five presents the conclusions and suggestions for future works.

CHAPTER 2

LITERATURE REVIEW AND THEORETICAL BACKGROUND

2.1 Introduction

This chapter reviews pertinent and relevant literature, general theories and principles that govern the subject matter of this study. The basic intrinsic characteristics of the ZnO, and their synthesis approaches are concisely explained. Afterwards, the effects of metal-doping and synthesis parameters on the crystal structure and optical properties of ZnO nanostructure were reviewed. The synthesis of Al-doped ZnO, the chemical bath deposition method used in this study and other conventional synthesis techniques of ZnO were also described. In addition, a synopsis, and basic principles of RL with tunability elements are outlined. Furthermore, the effects of aluminum doping on RL emission and the effects of incorporating SiO₂ layer on the optical properties of ZnO were reviewed. Lastly, this chapter elucidates the properties and applications of the RL.

2.2 Fundamental Properties of ZnO

ZnO is n-type semiconductor practical material, which has potential application in the ultraviolet or blue range of the spectrum due to its large band gap (3.37 eV). The exciton binding energy (60 meV) of ZnO enables the production of efficient excitonic emission under ambient conditions [47]. The generation of ultraviolet luminescence at room temperature has been reported in ZnO thin films and nanostructures [48–50].

The applications of ZnO have been expanded based on its piezoelectric and semiconducting properties, as a photoconductor [51], field-emitter [52], logical gate

[53], and wave-guide [54]. In recent times, ZnO has garnered research interest in energy conversion applications such as dye sensitized solar cells [55], and gas sensors [56]. Morphological variations of ZnO nanostructures include NRs, nanobelts, nanocombs, nanowires, and others. Moreover, the facile synthesis and growth of ZnO using an array of methods on an extensive variety of substrates improves its potential for the manufacture of future devices. Since the applications and future prospects of ZnO are based on their physical properties, their structural and optical properties are discussed in the underlying subsections.

2.2.1 The Crystalline Structure and Lattice Parameters

As a member of II-VI binary semiconductor materials, ZnO are present in the forms of either zinc blende or hexagonal wurtzite, where each anion (group-II atom) is encircled or decorated by four cations (group-IV atom) at each angle of a tetrahedron [57–59]. This tetrahedral coordination is a characteristic feature of sp^3 covalent bonding. The semiconductor materials also display an extensive ionic character and tend to expand the band gap. There is an alternate stacking of the cation (O^{2-}) and anion (Zn^{2+}) along the c-axis, thereby creating a decentralized symmetric structure with polar symmetry along the hexagonal axis that indirectly influences the piezoelectric feature and spontaneous polarization, in addition to crystal growth, defect formation, and etching of ZnO. The common crystal structures of ZnO are wurtzite (B4), zinc blende (B3), and rock-salt (or Rochelle salt) (B1), as presented in Figure 2.1. At ambient conditions, wurtzite (B4) is the thermodynamically stable crystal phase of ZnO. The hexagonal lattice of wurtzite is a member of the space group, $P63mc$, in the Hermann-Mauguin notation and space group C^4_{6v} in Schoenflies' notation with two lattice parameters $a = 0.3269$ and $c = 0.52065$ nm having a ratio $c/a = 1.60$ in an ideal wurtzite

structure. The wurtzite structure comprises two interconnected hexagonal-close-packed (hcp) sublattices, with each consisting of one kind of atom dislocated around each other along the 3-fold c -axis by a magnitude of $\underline{u} = 3/8$ (i.e. 0.375) for an ideal wurtzite structure.

The internal parameter of u is described as the length of the bond parallel to the c -axis (bond length between anion and cation or the closest neighbor distance) divided by the c lattice parameter, in unit of c . In a realistic scenario, the wurtzite structure of ZnO deviates from the model design as the c/a ratio or u value changes. The c/a is strongly dependent on u in a way that the u parameter decreases when c/a increases, while the four tetrahedral distances remain constant in the course of the deformation in tetrahedral angles as a result of lengthy range polar interaction. The stability of zinc blende is only achieved when ZnO is synthesized on a cubic structure, whereas rock-salt structure needs high pressure to be created with epitaxial stability unattainable. The basic physical parameters of ZnO are summarized in Table 2.1.

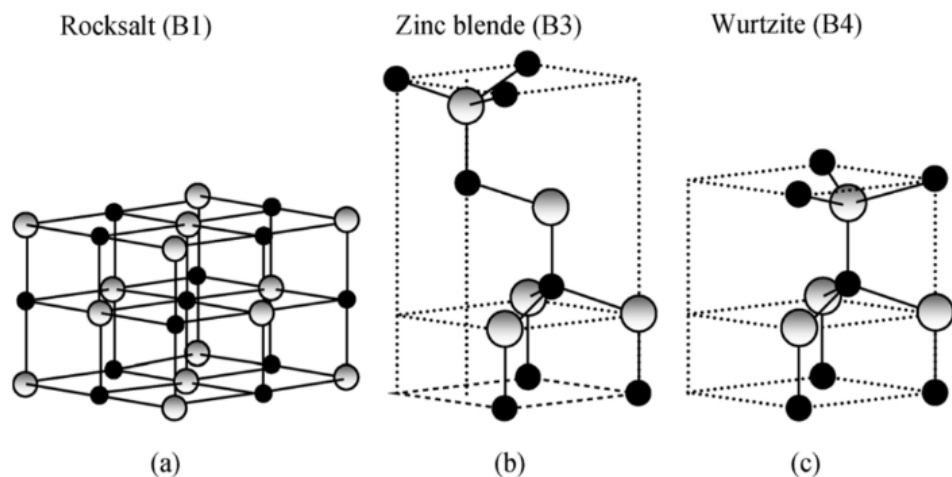


Figure 2.1: Stick-and-ball representation of ZnO crystal structures. (a) cubic rocksalt (B1), (b) zinc blende (B3), and (c) wurtzite (B4). Shaded gray and black spheres denote Zn and O atoms, respectively[57].

Table 2.1: Summary of the basic physical parameter of ZnO [60].

Physical parameters	Values
Lattice parameters at 300 K	
a	0.3269 nm
c	0.52065 nm
c/a	1.60
Density	5.606 g/cm ³
Stable phase at 300 K	Wurtzite
Melting point	1975 °C
Thermal conductivity	0.6, 1-1.2
Linear expansion coefficient (/°C)	a: 6.5×10 ⁻⁶ / c: 3.0×10 ⁻⁶
Static dielectric constant	8.656
Refractive index	2.008, 2.029
Energy gap	3.37 eV, direct
Intrinsic carrier concentration	<10 ⁶ cm ⁻³ (max n-type doping>10 ²⁰ cm ⁻³ electrons; max p-typedoping<10 ¹⁷ cm ⁻³ holes>)
Exciton binding energy	60 meV
Effective electron mass in conduction band, m_e	0.27 m _o
Electron Hall mobility at 300 K for low n-type conductivity	200 cm ² /V.s
Effective hall mass in valance band, m_h	1.8 m _o
Hole Hall mobility at 300 K for low p-type conductivity	5-50 cm ² /V.s

2.2.2 Optical Properties

Both intrinsic and extrinsic effects significantly influence the optical properties of a semiconductor [58,61]. Intrinsic optical transition occurs between the electrons and holes in the conduction and valence bands, respectively, with the addition of excitonic effect resulting from Coulomb interaction. On the other hand, extrinsic

transitions are associated with the localized electronic states generated in the bandgap by dopants/impurities or point defects and complexes, which affects both processes of emission and optical absorption. Excitons are categorized into free and bound excitons [62–64]. Bound excitons are those excitons that are affixed to the neutral or charged donors and acceptors. There is a strong dependence of electronic states of bound excitons on the semiconductor material, particularly the band structure.

The optical and refractive properties of ZnO have been exhaustively researched starting from Thomas in 1960's, who explored the basics of absorption edges and exciton structure of ZnO [62]. The invigorated attention on the properties and applications of ZnO nanostructure is propelled by its potential utilization in the manufacture of optoelectronics due to its direct wide band gap (3.37 eV) under ambient conditions, considerable exciton binding energy (60 meV) and efficient radiation recombination. The wide direct band gap of ZnO implies that it covers both blue-UV emission and large exciton binding energy which enables effective excitation emission at low excitation energy under ambient conditions.

The optical properties of ZnO (optical absorption, transmission, reflection, photoluminescence (PL), photo reflection, spectroscopic ellipsometry, cathodoluminescence, calorimetric spectroscopy) synthesized using different techniques have been explored. However, emphasis is given only to photoluminescence because it is a key component of this thesis. The properties of semiconductors can be subjected to changes to produce the 'quantum confinement effects' when minimized to the nanometres size. Based on photoluminescence data, quantum confinement can increase the energy band gap of ZnO [65,66]. PL is generated by the radiative recombination of free and bound excitons. PL spectrum

normally displays two emission bands (UV and broad emissions) under ambient conditions [67–71]. UV emission band is associated with a near band edge (NBE) transition of ZnO, which denotes the recombination of free excitons. In addition, a broad emission band is observed between 420 and 700 nm in almost all samples irrespective of the synthesis method and growth factors. This emission discernible in the visible region is referred to as deep level emission (DLE) which is attributable to defect formation and the presence of impurities in the crystal structure such as O-vacancy, Zn-vacancy, O-interstitial, Zn-interstitial, and extrinsic impurities like substitutional Al. It has been reported that the green band emission evident in the region of 520 nm is indicative of the singly ionized oxygen vacancy in ZnO and is generated by the recombination of a photo-generated hole with the singly ionized charge state of this defect.

2.3 Methods to Synthesize ZnO Nanostructures

Nanotechnology has vastly advanced, leading to the growth of 1D ZnO structures that are potentially relevant to the manufacture of optoelectronics. The most common techniques of fabricating ZnO include vapour and solution phase syntheses. The vapour phase technique generally requires a vacuum chamber under gaseous settings set at a high-temperature range of 500 - 1500 °C. This technique synthesizes very high quality, single-crystal ZnO nanostructure, although synthesis factors and parameters such as gas species, evaporation duration, flow rate, pressure and temperature must be precisely tuned. The vapour phase technique can be further classified into physical vapour deposition (PVD) and chemical vapour deposition (CVD) [72]. PVD involves the physical release of the material to be deposited from a precursor or source and subsequent transfer to a substrate in the absence of chemical

reactions. Classic examples of PVD include molecular beam epitaxy (MBE) [73], pulse laser deposition (PLD) [74] and sputtering. On the other hand, CVD utilizes the chemical reactions that occur between the volatile precursor and vaporized material. The CVD techniques include metal-organic chemical vapour deposition (MOCVD) [7], metal-organic chemical vapour phase epitaxy (MOVPE) [75] and plasma-enhanced CVD (PECVD). Because of the need for precise control of the synthesis process, these techniques are preferable for the production of ZnO nanostructures. However, the process is intricate and tedious, and requires advanced equipment and high operational temperatures, in addition to the toxic chemicals associated with the process. These constraints deter large scale production of ZnO nanostructures for commercialization.

On the contrary, the solution-phase technique (e.g. electrochemical deposition (ECD) [76], sol-gel synthesis [77] and chemical bath deposition (CBD)) requires low temperature for synthesis (normally $< 300^{\circ}\text{C}$). This immense benefit expands the variety of shapes and kind of substrates that can be utilized such as flexible-stretchable substrate, temperature sensitive substrates, and fibers [78]. Other advantages include facile experimental system, cost-effectiveness of the process, and high potential for up-scaling. Apparently, this technique also has some drawbacks, particularly the tedious process of tuning the morphology of the nanostructure because the entire process underpinning the growth of nanostructures has not been thoroughly elucidated.

2.3.1 Chemical Bath Deposition

CBD is the most basic and versatile solution growth technique. CBD has also been referred to as chemical solution deposition, liquid phase deposition, chemical deposition and aqueous solution method. CBD generally entails the synthesis in

solution, which involves oxide deposition and hydrolysis of metal cations. It requires low growth temperature of $< 300\text{ }^{\circ}\text{C}$, which expands the variety of shapes and kind of substrates that can be utilized. Other advantages include facile experimental system, cost-effectiveness of the process, and high potential for up-scaling. A numerous studies have explored the synthesis of ZnO nanostructures using chemical bath deposition [4]. The data is indicative of the mounting scientific interest on the synthesis of ZnO using CBD. However, this inclination is simply qualitative, while the variables related to CBD are underemphasized. The use of CBD to synthesize ZnO NRs with lasing properties have only recently been established [15]. This thesis primarily focuses on the use of CBD with doping to determine changes in RL by maintain the average size of NRs and only make changes in Al doping ratio.

Several endeavours have been dedicated to develop guidelines, procedures and chemical combinations for synthesizing high quality films and well orientated ZnO nanorod array. Incorporating a seed layer before the growth process is one of such efforts. In addition, different thicknesses of ZnO seed layer have been deposited on Si substrate using the sputtering technique prior to CBD [79]. It was observed that the average diameter of ZnO NRs vertically deposited on the substrate was proximate to the average grain size of ZnO thin film [79]. ZnO has also been prepared through the combination of MOCVD and CBD, where MOCVD was used in synthesizing the seed layer [80]. The crystal structure, morphology, and growth rate of the ZnO NRs was found to be strongly dependent on the thickness and structure of the seed layer. The two-step CBD was proven to be the most effective approach for controlling size and alignment of the ZnO NRs [81]. Therefore, the two-step CBD technique with the incorporation of a seed layer was adopted for this research.

Furthermore, hexamethylenetetramine (HMT) serves the vital role of controlling the growth of ZnO NRs in the CBD process. HMT is a water-soluble tertiary amine characterized by a symmetric tetrahedral cage-like structure with four nitrogen atoms (N) at the four edges and six methylene bridges ($-\text{CH}_2-$). HMT plays a dual role of donating OH^- ions and as a capping agent to promote anisotropic growth [4]. The length of ZnO NRs is directly proportional to the supersaturation in solution, which in turn is dependent on the concentrations of HMT and $\text{Zn}(\text{NO}_3)_2$ as well as pH of precursor solution [82]. Morphological characterization of the ZnO NRs using FESEM indicates that their diameter and lengths decreased with increase in the concentration of HMT. Nonetheless, a different study reported that the concentration of HMT does not interfere with the growth rate of ZnO NRs [83]. Similarly, the nanowire growth was observed to not involve the adsorption or incorporation of HMT [84]. Alternatively, HMT offers the required thermodynamic stability of the crystal growth process, whereby the OH^- ions are gradually released.

Time, temperature, and precursor solutions are factors that influence the CBD process. An appropriate blend of these parameters is important to achieve high quality NRs. These parameters have been varied in a number of studies to modify the alignment of ZnO nanostructure. For instance, Idiawati et al. demonstrated that the length and diameter of NRs can be increased by raising the growth duration from 4 to 8 hours, [85]. Nandang mufti et al. reported that temperature range of 80 - 90 °C is the most suitable range for the CBD process, according to the morphology, crystal structure and optical properties of the synthesized ZnO NRs [86]. The nanosize and morphology of controllable ZnO NRs deposited on glass substrates were achieved by controlling the concentration of the precursors [87]. Thicker and longer NRs with

improved crystallinity and visible emission intensity were observed as concentration of the zinc precursor was increased, although the density of NRs decreased.

2.4 Metal-doped ZnO Properties

Doping is the process of incorporating specific impurities (dopants) to a semiconductor [88]. It is a critical approach for improving and tuning the crystal structure and optical properties of ZnO nanostructures [89]. Although ZnO naturally exhibits n-type doping, the source of electrons that provides this effect is arguable. This n-type behavior has mostly been attributed to point defects and interstitials. Hence, p-type doping is hard to achieve in ZnO as a result of the self-compensation effect of ZnO by native point defects [90]. Essentially, veritable doping elements should have ionic radius proximate to that of host ion in order to preserve the lattice structure and must also have close electronegativity to dynamically support its inclusion into the lattice [91]. ZnO nanoparticle can be controlled by doping with group III element such as Al [92], In [93], Ga [94]. Al, Ga, and In are good shallow and effective donors when they substitute Zn in accordance with the equation 2.1 [91]:



Where D^0 and D^+ denote the neutral and ionized donors, respectively, and the equilibrium under ambient conditions is basically on the right-hand side of the equation.

2.4.1 Al-doped ZnO Nanostructures

Al is an exceptional dopant for ZnO because it has a single positive Al^{3+} , which has a smaller ionic radius compared to Zn^{2+} [95]. It is also more suitable to occupy the interstitial site. Moreover, Al doping improves the resistivity, high transmittance in the visible light region and thermal stability of the ZnO nanostructure. Several techniques have been explored for the synthesis of Al doped ZnO thin film. The effects of concentration on the properties of ZnO thin film have been researched in detail [96–98]. However, the growth or synthesis parameters of ZnO thin film such as solution molarity, dopant source and concentrations solutions, heating temperature and time, type of substrate, annealing temperature and duration of synthesis remain debatable, particularly in terms of structural, optical, and electrical properties. Edinger et al. synthesized ZnO doped with Al, Ga, and In, using the CBD method. The properties of the doped ZnO was found to be linearly dependent on the concentration of dopant in the solution, and Al doped ZnO exhibited the widest band gap of 3.50 eV [99]. On the other hand, a different study reported that the band gap of Al doped ZnO (3.16 eV) synthesized using spin coating is relatively smaller than that of Ga doped ZnO (3.26 eV) [100]. Nonetheless, both groups displayed over 80% transparency in the visible region. Furthermore, Baka et al. posited that the optical band gap of ZnO increase from 3.22 eV to 3.47 eV with increased in concentration of Al [100].

2.4.1(a) Effects of Al-Doping on The Morphological Properties

The Al doping concentrations play an important role on the morphological properties of ZnO nanostructures. J.T. Chen et al. reported the synthesis of undoped and Al-doped ZnO nanostructures fabricated by combining the sol–gel spin-coating and the hydrothermal process [101]. They discovered that when ZnO was doped with

Al (6 at.%) percent, the morphology changed dramatically from nanorods to nanosheets, which is caused by the deterioration of ZnO orientation growth at high concentrations of $\text{Al}(\text{OH})_4^-$. Cheng et al. revealed that the $\text{Al}(\text{OH})_4^-$ complex impeded the growth of ZnO along the (0 0 2) plane and the fabrication of ZnO nanoplates with increasing Al on substrates [102]. Another study investigated the influence of Al doping on the morphology of ZnO nanopowders. The shape of ZnO nanopowders changes from flower structure to sheet-like structure as the amount of Al doping increases [103].

M. Advand et al. investigated the influence of Al-doping on the material properties of the ZnO NRs array produced by the hydrothermal growth process [33]. According to the research, by changing the Al doping, remarkable changes in the morphology of ZnO NRs were observed. By increasing the Al doping from 1 to 7 wt%, the diameter of the NRs increases as shown figure 2.2 and 2.3. Significant distortion is detected along the growth direction (c-axis), implying that increasing the Al concentration caused the vertical ZnO NRs to change into ZnO nanoplate structures.

N. Fadzliana et al. presented work of AZO NRs fabricated on ITO coated glass substrates using simple chemical deposition technique and the morphological results showed a decreasing of the population density of the nanorods trend with increasing dopant concentration from 153 NRs/ μm^2 to just 53 NRs/ μm^2 at 50 mM doping concentration [26]. A decrease in growth rate when more Al dopants are introduced due to the presence of $\text{Al}(\text{OH})_4^-$ impeding the growth along the c-axis as well as decelerating of growth by the pronounced precipitation of the solution.

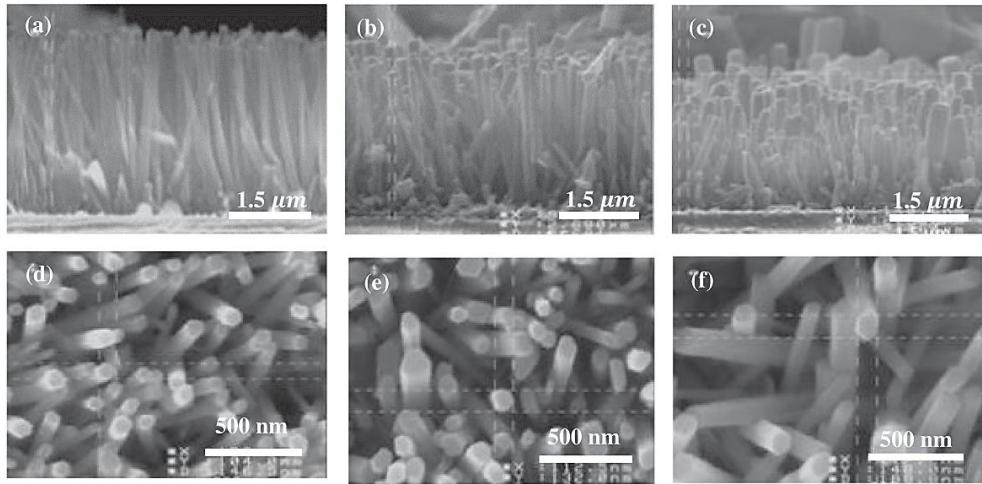


Figure 2.2: FESEM cross-sectional and top-view images of ZnO nanostructures doped with (a, d) 1% Al; (b, e) 3% Al. (b) [33].

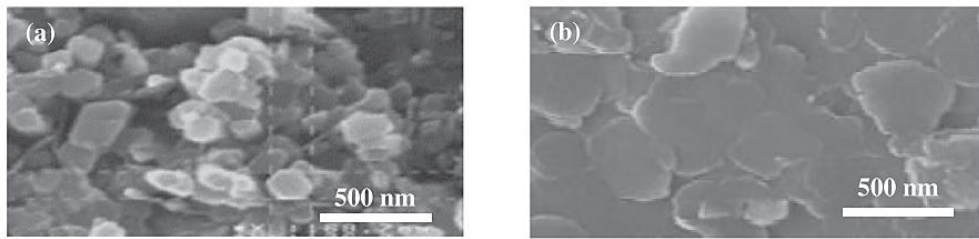


Figure 2.3: FESEM images of the surface morphology of ZnO nanostructures doped with (a) 5% and (b) 7% Al [33].

2.4.1(b) Effects of Al-Doping on The Optical Properties

As noted in section 2.2.2, the optical characteristics of ZnO can be determined using the non-destructive PL spectroscopy [104], [105,106]. The PL spectra of ZnO generally comprises a distinct ultraviolet (UV) emission at 378 nm attributed to recombination of free exciton and visible (green) emission mainly denoting oxygen vacancies (V_o) [48]. Bahedi investigated the crystal structure, morphology, optical and photoluminescence properties of ZnO thin films doped with varying concentration of Al (0 wt% to 10 wt%) via spray pyrolysis. The intensity of the UV peak in PL spectra is higher for the doped samples particularly for Al concentration of 3 wt%. The

increase in intensity of UV emission was found to be consistent with the improvement of crystal quality [107]. However, conflicting data on the green emission attributable to Al have also been reported. Based on the results reported by Thomas et al., the green emission is improved with Al substitution due to the larger charge density of Al in the addition to the V_o generated in the process [108]. Geng et al. reported a decline in ZnO band edge emission as the concentration of Al dopant is increased, indicating weaker crystalline quality [109].

2.5 Random Lasers

To comprehend RL, there is a need to understand conventional lasers. The laser is the abbreviation of “Light Amplification by Stimulated Emission of Radiation”. It is an optical device that emits light that was amplified by a resonator. Einstein presented a calculation for probabilities of absorption and stimulated emission of quanta from the electromagnetic beam in 1917 [110]. After Einstein hypothesized the process of stimulated emission, the creation and advancement of laser quickly evolved. In 1960, the first laser was demonstrated by Theodore Maiman by focusing a high-power flash lamp as a pump source on a 1 cm sized ruby crystal coated with silver on two parallel faces [111].

Three kinds of interaction occur between the light and gain medium during the lasing process. Firstly, absorption arises as an electron is excited from the ground state to a higher energy state because of the pump light. This is accompanied by spontaneous emission where the excited electron is reversed to the ground state and a photon is emitted. Thirdly, a stimulated emission takes place. Here, the photon emission (resulting from the reversal of the electron to ground state) is stimulated by an incident photon. Two photons with same phase are emitted in this stimulation process. A

conventional laser typically comprises an energy source, a gain medium, and an optical cavity. The energy source is derived from a ‘pumping’ process and can be provided through an electrical current or another light source. A gain medium is a material that supplies optical gain by means of the stimulated emission, and the optical cavity partly captures the light. Fabry-Perot is a well-known conventional laser, as illustrated in Figure 2.4 (a). The gain medium is positioned inside the cavity with two mirrors (one is partially transmitting) placed at both ends of the gain medium to capture the light. In Fabry-Perot laser, as the light is transmitted through the first mirror, it travels through the gain medium and hits the second mirror. The light bounces backward and forward in the cavity which travels through the gain medium each time, thus stimulating additional photons in each course. The system achieves a threshold when the total gain in the cavity exceeds the losses, and a photon beam is released referred to as the laser output. For a conventional laser, the laser output is narrow emission lines that are uniformly separated with a fixed mode spacing ($\Delta\lambda$), which indicates mode resonant cavity as depicted in Figure 2.4 (b) [112].

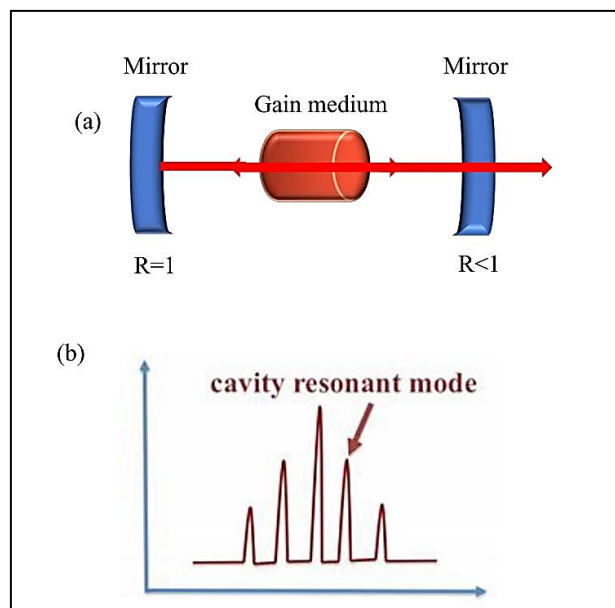


Figure 2.4 : (a) Schematic diagram of Fabry-Perot laser consists of two mirrors and gain medium (b) laser output for conventional laser [112].

2.6 Key Principles of Random Laser

2.6.1 Gain Medium

According to the principle of RL operation, there are two basic elements in the RL system: scatterers (e.g., powders, biological tissue, nematic liquid crystal), and the gain material (e.g., laser dye, quantum dots). Nonetheless, certain active scatterers (e.g., semiconductor, rare earth doped powders, polymer matrices) can offer both scattering and gain, simultaneously, by means of special design and fabrication. Semiconductor is a viable option as lasing gain media because of its inherent different bandgaps; hence several semiconductor materials have been considered as precursor materials for the fabrication of RL since the inception of RL theory.

Structural varieties (powders, nanowires, NRs, nanoneedles) of ZnO [113–115], ZnSe[116], ZnS [117], GaAs [118], GaN[119], SnO₂[120], etc. have been utilized as both scatterers and gain media in RL. Generally, semiconductor powder crystals synthesized via re-crystallization travelling-heater method are crushed to micron size [4].

Submicron sized rare earth powders are another active medium which are prepared from rare earth doped crystals or glasses. This method facilitates both the scattering and gain functions concurrently. For example, Nd³⁺ doped active powders have garnered considerable attention in the context of RLs because of its low threshold and high efficiency [121–124].

Laser dyes are organic molecules that are extensively utilized as a laser gain media. Laser dye-based RLs have been fabricated using active scatterers such as ZnO [125], passive scatterers as TiO₂ powders [126], nematic liquid crystals [127,128],

biological tissues [129,130], etc. The dye-doped nematic liquid crystal RL is one of the most basic systems. Its fabrication entails the addition of laser dye to a nematic liquid crystal to produce a colloidal solution that can provide both scattering and gain, thus enabling random lasing. By applying the multiphoton up conversion, RL can also be achieved using the colloidal solution of passive particles (TiO_2) and laser dye [131]. The combination of the metal particles and dye also been used as the active gain media [132,133]. By applying the self-assembly technique, the laser dye can be confined into polymer nanoparticles which can enable both scattering and gain. Hence RL is observable in the dye-doped latex nanoparticles [134] and dye-doped POSS solutions [135]. Generally, biological tissues from vegetable, animals, and human organs can naturally comprise disordered nanostructures, thus they can be utilized as the scattering media devoid of any post-processing[136]. As laser dye infiltrates the biological tissue, the induced RL action can distinguish the malignant tissues from healthy ones. However, the use of dyes comes with other problems such as dye degradation (especially if pump power is high), the need to always replace laser dye for repeated measurements and dealing with dye wastes [137] [138][138]. For a more sustainable gain medium, researchers have moved to solid state gain medium specifically semiconductor solid state gain mediums [113,116,124,139].

2.6.2 Coherent and Incoherent of Optical Feedback

The trapping of scattered light to form a closed loop in disordered nanostructures result in coherent feedback. Thus, for a coherent feedback RL system, the interference effect arises from the closed loop. Its key feature is the laser spikes (very narrow emission lines) in the spectral emission [113],[140], which is the primary disparity between the features of a RL with a coherent feedback and that with